**THE EUROPEAN
PHYSICAL JOURNAL D**

Regular Article

Magnetic coherence gratings in a high-flux atomic beam

A. Tonyushkin[a], A. Kumarakrishnan[b], A. Turlapov[c], and T. Sleator

Department of Physics, New York University, 4 Washington Place, New York NY 10003, U.S.A.

Abstract. Magnetic coherence gratings have been created in a thermal beam of rubidium atoms. The coherence gratings involve superposition of magnetic sublevels of a single hyperfine ground state. These gratings are created via interaction with a single pulse that drives a two-photon transition between magnetic sublevels of the ground state. After the grating dephases due to the velocity distribution of the atoms, it is revived by the action of a second pulse, an effect that is similar to a photon echo. Such experiment is a first step toward generating periodic atomic structures using a high-flux atomic beam. Here, we present the experimental results and provide a detailed description of the apparatus that produces a high flux beam of thermal rubidium atoms.

1 Introduction

Over the last several decades, laser light has been used to coherently manipulate atoms in a variety of experiments [1]. One of the interesting applications of coherent control involves coherent transient effects in atomic systems [2–6] in a similar fashion as rf fields are used in nuclear magnetic resonance spectroscopy in liquids and solids [7–11]. In atomic systems these effects lead to the formation of spatially dependent coherences between internal atomic states. Examples include magnetic grating free induction decay (MGFID) and magnetic grating echoes (MGE) from ground states of Rb atoms that are either laser cooled [12,13] or at room temperature [14]. A number of recent theoretical proposals on the super-resolution quantum lithography schemes that utilize internal states coherences [15–17] show potential practical importance of the internal states coherences in the appropriately chosen atomic medium. Spatially dependent coherences created in a lambda-type medium can be used as the basis for arbitrary patterning techniques in quantum optics [18–20].

We have used a photon-echo-type technique [21–24] to create a magnetic-states coherence grating in a high-flux rubidium atomic beam [25]. The ground-state coherent echo technique was theoretically developed in reference [2]. In that proposal, the coherence between ground-state

[a] *Present address:* Department of Physics, Harvard University, Cambridge, MA 02138, USA; e-mail: at402@nyu.edu
[b] *Present address:* Department of Physics and Astronomy, York University, 4700 Keele Street, Toronto, Ontario M3J1P3, Canada.
[c] *Present address:* Institute of Applied Physics, Russian Academy of Sciences, ul. Ulyanova 46, N. Novgorod, 603950, Russia.

magnetic sublevels is created by the action of two laser fields with opposite polarizations and k-vectors $\mathbf{k}_1$ and $\mathbf{k}_2$. The same interaction simultaneously creates a periodic spatial modulation of the coherence that has a period $2\pi/|\mathbf{k}_2 - \mathbf{k}_1|$, therefore, producing a coherence between momentum states associated with atomic center of mass motion. In the presence of Doppler dephasing the established coherence quickly vanishes, however, the second pulse reverses the phase of coherence, which is completely rephased at a specific time known as the echo time. The lowest order harmonic of coherence can be probed by coherently scattering a probe beam off the periodically modulated coherence grating.

In our experiment, a spatially modulated coherence was created between the magnetic sublevels of the $F = 3$ ground state in ^{85}Rb by an excitation pulse consisting of two counter-propagating orthogonally polarized traveling waves. These gratings were detected by coherently scattering a weak probe beam off the grating. Shortly after application of the laser pulses, the signal, refereed to as MGFID, decays due to dephasing of Doppler-broadened sample. We studied the dynamics of the MGFID in the presence of an external homogeneous magnetic field. In addition, the laser beams were aligned with an angle of a few milliradians to form a grating with a spatial period greater than the period standing wave (i.e., to increase the lifetime of the gratings).

Magnetic grating echo is closely related to atomic population grating echo [26,27] created by application of off-resonant standing wave fields, which only affect atomic momentum states associated with the center of mass motion. The population grating echo in an atomic beam is particularly valuable for atomic pattern deposition since the substrate can be physically separated from the excitation region. In addition, echo techniques do not rely on sub

recoil collimation of the atomic beam, as opposed to conventional deposition techniques [28,29]. As a result, it is possible to achieve significantly higher beam flux, thereby reducing the deposition times from several hours [30] to a few minutes [31–33]. The other distinction of the population gratings echo technique is in its potential ability to overcome limitation on the periods of the grating. Placing the standing wave near a surface allows one to deposit a series of lines or spots with a period of standing wave $\lambda/2$ [28,29], where λ is the wavelength of light. There are several techniques that allow the creation of structures with smaller than a half wavelength periodicity. By using orthogonally polarized counter-propagating waves, structures with period $\lambda/4$ were deposited [34]. In a double exposure experiment in which the detuning was alternated from positive to negative, a $\lambda/(2\sqrt{3})$ periodicity was achieved [35]. These methods have relied mostly on the focusing of atoms in a standing wave located immediately adjacent to the surface of deposition. The echo technique allows to break this barrier: by choosing an appropriate time interval after the application of the second pulse, one can observe subwavelength periods $\lambda/2n$ for arbitrary integer n. Reference [27] describes the first experiments that used echo techniques to produce such periodic structures in a magneto-optical trap (MOT). Optical mask techniques for direct imaging of structures with up to $n = 5$ were demonstrated in references [36,37]. The limitation of echo technique on the contrast of generated atomic patterns is presented in references [27,38]. We note, however, that for practical purposes, such experiments need to be carried out with an atomic beam in spatial domain.

Here, we demonstrate a magnetic grating echo phenomenon in the atomic beam, which is a precursor of the experiment on creation of the population gratings in the thermal atomic beam.

2 Qualitative description of experiment

The experiment is based on a coherent transient effect described in reference [3]. The experiment is carried out in the time domain, however, the practical version of such a scheme would involve spatially separated continuous wave light gratings that would appear to be pulsed in the moving frame of the atomic beam. Figure 1 shows the configuration of the experiment. To create a coherence grating, the atomic beam is excited transversely by a pulse consisting of two traveling waves (TWs) with wave vectors $\mathbf{k}_1$ and $\mathbf{k}_2$ at a small angle θ ($\sim$few mrad). The TWs, with orthogonal linear polarizations, create a coherence grating involving adjacent magnetic sublevels of the ^{85}Rb $F = 3$ ground state $\Delta m = 1, 2, ..., 6$[1]. Figure 2 shows a level diagram for the atomic system. The coherence grating produced by the laser pulse, has a spatial periodicity $2\pi/\Delta k \sim 2\pi/k\theta$, where $\Delta k = |\mathbf{k}_1 - \mathbf{k}_2|$, $k = |\mathbf{k}_1| = |\mathbf{k}_2|$.

---

[1] For orthogonal circular polarizations of the excitation beams the coherence grating involves adjacent magnetic sublevels with $\Delta m = 2, 4, 6$.
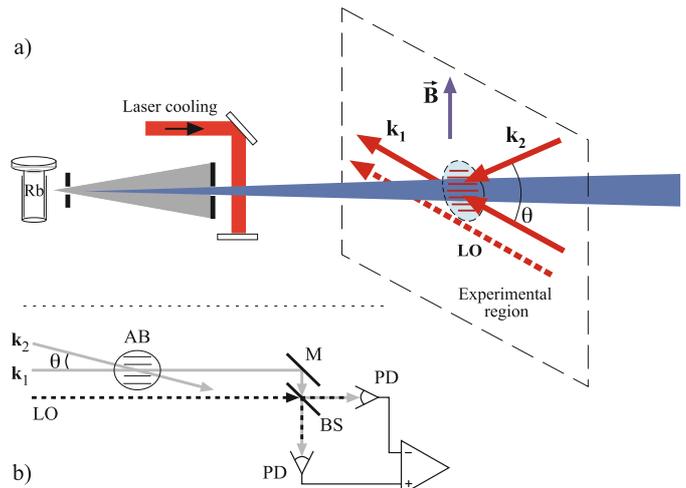
Fig. 1. (Color online) Schematic diagram of experimental setup: (a) configuration along the atomic beam; (b) heterodyne detection scheme, where LO = optical local oscillator field upshifted by 100 MHz from the excitation beams, AB = atomic beam (perpendicular to the plane of the figure), BS = optical beam-splitter, M = mirror, PD = photodiode (the quadrature demodulator is not shown).
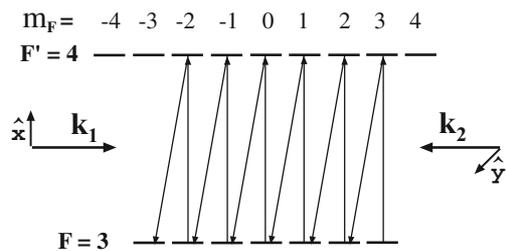
Fig. 2. A diagram of the magnetic levels structure of ^{85}Rb. The two-photon transitions for linear orthogonally polarized beams are shown by arrows.

This grating dephases due to thermal motion when the atoms move a transverse distance of the order of the grating spacing, i.e., on a time scale $2\pi/k\theta u$ where u is the rms component of velocity along the direction of grating vector $\Delta \mathbf{k}$. The dephasing of the grating is probed by a linearly polarized TW "readout" pulse along $\mathbf{k}_2$. This pulse has the same polarization as the excitation pulse along $\mathbf{k}_2$ and excites a coherent superposition of ground and excited states. The superposition radiates along the direction $\mathbf{k}_1$ (satisfying phase matching conditions) with polarization orthogonal to the readout pulse. The resulting signal is known as an MGFID. The dephasing time for the atomic coherence grating can, in principal, be used to infer the transverse velocity distributions of the atomic beam [14]. To obtain a revival of the grating at a later time we use an echo technique. The atomic beam is excited by two sets of similar laser pulses separated by time T. The first pulse creates a coherence grating between magnetic sublevels, which quickly dephases. The second pulse, applied at time $t = T$ after the first pulse, causes a reversal of Doppler phases of atoms so that the coherence grating is rephased at time $t = 2T$. Again, the rephased grating is probed by a
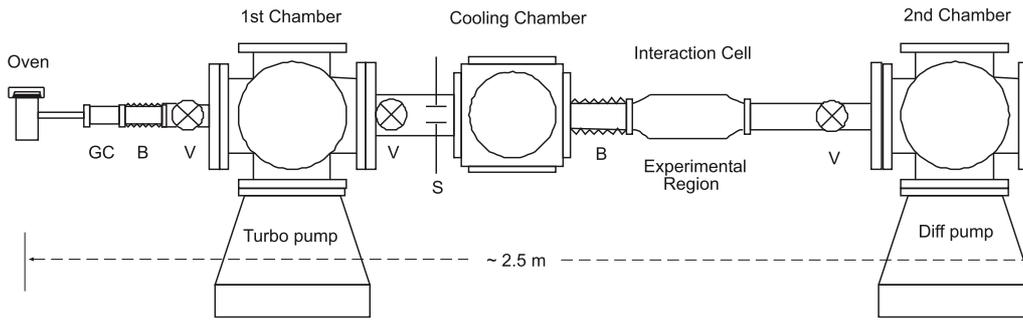
Fig. 3. Schematic of vacuum chambers of the atomic beam machine. Oven assembly is connected by bellows to the 6″ six-cross chamber, mechanical valves are used for venting the chamber, mechanically adjusted slit used for final collimation of the beam, a cube chamber is used for transverse laser cooling of the atomic beam, the interaction cell is connected by bellows to the 6″ cube, the second chamber is used for monitoring the atomic beam. Here, B = bellows, GC = glass cell, S = collimation slit, V = mechanical valve.

readout pulse. In this case, the coherently scattered signal from the sample is known as an MGE. The time scale of the echo experiment $(2T)$ is limited by the transit time of atoms through the interaction region [14]. For small angle excitation, the MGFID and MGE are not influenced by recoil effects. The MGFID exhibits Larmor oscillations in the presence of an external, homogeneous magnetic (bias) field oriented along the quantization axis defined by the polarization of the $\mathbf{k}_1$ beam. For the case of excitation by pulses with orthogonal linear polarizations, the modulation at the Larmor frequency can be attributed to the precession of magnetic dipoles in a magnetic field. The Larmor frequency is determined by the Zeeman splitting between magnetic sublevels of the ground state separated by $\Delta m = 1$ [12].

# 3 Experimental details

3.1 Experimental set-up

A schematic of the experiment is shown in Figure 1. The traveling waves of the excitation pulse are applied simultaneously with a typical duration $\sim 200{-}300$ ns. They are tuned to the $F = 3 \to F' = 4$ transition $(5S_{1/2} \to 5P_{3/2})$. The pulses are generated by two acousto-optical modulators (AOMs), which diffract light from a high-power diode laser. A common rf oscillator operating at 100 MHz is used to drive both AOMs. For detection we use a balanced heterodyne detection technique, which is schematically shown in Figure 1b. The signal is observed along $\mathbf{k}_1$ while applying a readout pulse along $\mathbf{k}_2$. The backscattered light representing the signal interferes with the undiffracted CW light from the $\mathbf{k}_1$ AOM, which serves as an optical local oscillator. The local oscillator is shifted 100 MHz above resonance and passes through the cell ~ 1 cm from the interaction region. The beating pattern of light intensity oscillating at a difference frequency of 100 MHz (beating frequency) is acquired by a pair of identical balanced silicon PIN photodiodes (~ 1 ns-rise time). The balanced differential detection is used to suppress the amplitude noise of the laser so that the signal-to-noise ratio is limited by the shot noise. The signal from the detector is mixed with a reference signal from the rf oscillator in a quadrature demodulator. The dc outputs of the demodulator, which represent the real and imaginary amplitudes of the scattered electric field, are recorded on a digitizing oscilloscope. The pulse sequence and delay times were controlled by electronic delay generators.

To detect the MGFID signal we used a weak 6 μs-long readout pulse to record the entire decay of the signal. The decay time of the signal was obtained by averaging the signal over a few hundred repetitions of the experiment.

3.2 Vacuum chamber

The atomic beam apparatus consists of a rubidium oven and a vacuum system with several differentially pumped interaction zones as shown in Figure 3. The pressure in the chamber is monitored by several ionization gauges tubes. The first chamber is connected to a turbo pump with pumping speed of 10 L/s. This chamber is used for monitoring the atomic beam and background density by probing absorption. There is a mechanically adjustable collimation slit between this chamber and the optical cooling chamber. In this region, transverse laser cooling is implemented along either the horizontal or vertical dimension depending on the direction of the grating vector $\Delta \mathbf{k}$. The coherent transient experiments are carried out in an interaction cell consisting of a rectangular quartz tube with a square cross section. The interaction glass cell is located between two differentially-pumped chambers and connected to the cooling chamber using a bellows assembly. In some of the experiments, such as the measurement of the effect of a magnetic field on coherences (see Sect. 4.2), a 2 3/4″-flange ConFlat stainless steel chamber was used instead of glass cell. The second chamber in Figure 3 is located at the end of the vacuum assembly and connected to a diffusion pump. The two vacuum pumps maintain a background pressure in the system of $\sim 10^{-7}$ torr. The second chamber is used to monitor the atomic beam flux. The efficiency of laser cooling is also monitored in this chamber using a time of flight technique.
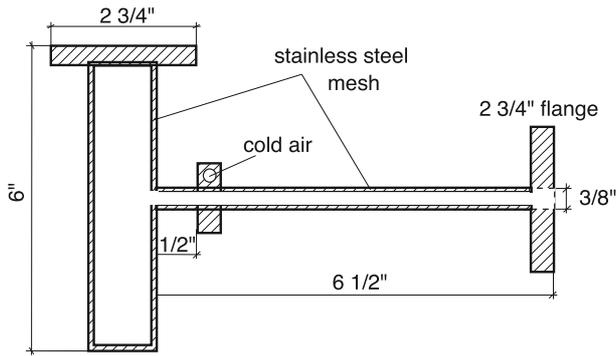
Fig. 4. Recirculating oven and tube assembly design (the dimensions given in inches and represent standard stainless-steel ConFlat flanges).

3.3 Oven assembly

The experiment described in this work utilized a recirculating rubidium oven. The atomic beam is produced using a custom made tube that has a design similar to [39,40]. The schematic of the reservoir and tube assembly is drawn to scale in Figure 4. A fine stainless steel mesh is wrapped inside the reservoir and the tube, thus providing the reflux mechanism for the rubidium mass flow based on the capillary effect. The reservoir is heated through a spirally wound thermal coaxial element and the temperature is controlled using a variable transformer. Additionally, the reservoir is insulated with fiberglass strips. The temperature, ranging from 240° to 300 °C as measured by the outside thermocouple sensor, is sufficient to achieve the beam flux of $\sim 1 \times 10^{12}$ atoms/(s cm²). The tube end of the oven is cooled with compressed air flow around the external surface near the oven aperture. The relatively cold tube wall limits rubidium vapor emission in the vicinity of the aperture and prevents collisional losses that can reduce the atomic beam flux through the long tube. The lifetime of the oven was estimated to be several months of continuous operation, which represents a significant improvement compared to a previously used non-recirculating oven.

The oven assembly is connected to a cylindrical glass cell (see Fig. 3) to allow visual inspection of possible problems with the rubidium at the exit of the tube. This glass cell is connected to a bellows assembly that serves as the pivot point of the oven assembly. The oven reservoir rests on a two-dimensional translational stage that is used to align the atomic beam direction inside the vacuum system. After each run the oven tube assembly is allowed to cool down to just above the melting point of rubidium. It is then tilted with respect to the axis of the vacuum system by $\sim 30°$ to help recirculate rubidium inside the oven.

3.4 Atomic beam characteristics

To measure the velocity distribution of the thermal atomic beam we performed absorption spectroscopy. We used a weak probe laser beam that is split into two paths: one
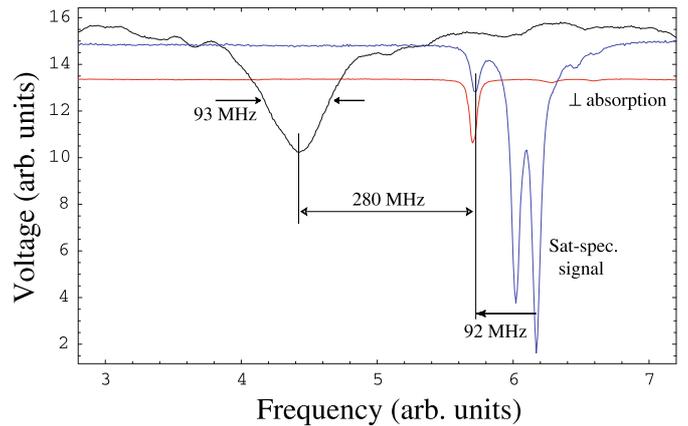
Fig. 5. (Color online) Atomic beam absorption spectroscopy: the broad black trace is an absorption at the angle 25.6° to the propagation axis of the atomic beam; the red trace ($\sim$280 MHz away) is the absorption nearly perpendicular to the beam axis; the blue trace is a saturated spectroscopy trace from the reference Rb cell.

part passes through the atomic beam perpendicular to its direction of propagation; the other path passes through the atomic beam at an angle of $\sim$25.6° to the propagation axis. The laser frequency was scanned over the hyperfine manifold of ^{85}Rb $F = 3 \rightarrow F'$. The resulting absorption spectra were detected by a photodiode and recorded on an oscilloscope. These traces were compared to the Doppler-free saturated absorption spectroscopy spectra obtained from a Rb vapor cell at room temperature that serves as a reference. Figure 5 shows the spectral features. The peaks in the atomic beam absorption traces correspond to the strongest (Doppler broadened) transition $F = 3 \rightarrow F' = 4$. Spectra from the reference cell allowed us to calibrate a frequency scale with a precision of 1 MHz. The Doppler shift between the two probe beams passing through the atomic beam and the Doppler broadening associated with velocity distribution of the beam were measured. From the frequency shift we obtained the most probable longitudinal velocity of the atomic beam to be $v_{\parallel} \approx 487$ m/s. The FWHM of the velocity spread $\Delta v = 168$ m/s. Therefore, the characteristic parameter of the velocity distribution, which defines the dynamics of the atomic beam, was $\Delta v / v_{\parallel} \sim 0.35$.

The absorption depth in the direction perpendicular to the atomic beam also allows the atomic beam density to be measured. The typical optical depth in the experiments was OD $\sim 0.1 - 0.4$.

4 Results and discussion

4.1 Magnetic-grating free induction decay

Here we present the experimental results related to creation of magnetic sublevel coherence gratings in an atomic beam. All the results discussed in this section were obtained in experiments where the excitation pulses are applied at a small angle ($\sim$100 mrad) to each other (see
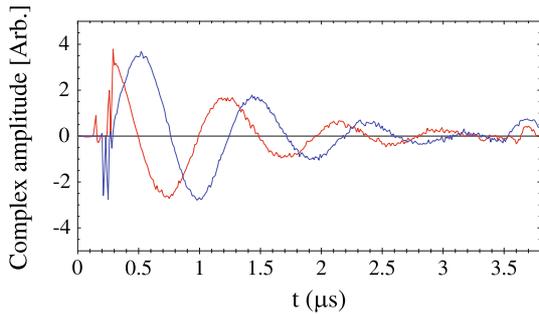
Fig. 6. (Color online) Raw data of the MGFID trace. Red and blue traces correspond to two quadrature components of the signal (note that the first 250 ns in the graph correspond to the excitation pulse itself). The oscillations are due to the external magnetic field of 3 G.


Fig. 7. MGFID signal, experimental data with a Gaussian fit according to a theory. The vertical scale is the absolute value of the amplitude, the horizontal scale is the time (the first 350 ns correspond to the pulse itself). Decay time from Gaussian fit is 0.79 μs.

Fig. 1). An example of the raw traces of the MGFID signal is shown in Figure 6. These signals were obtained with a collimation aperture of ~4 mm (see Fig. 1a) in the presence of one-dimensional cooling. The excitation pulses and the readout pulse are turned on at $t = 0$. The two traces represent the in-phase and quadrature components of the electric field that is coherently scattered from the sample. The readout pulse is a weak TW pulse with a duration of 6 μs. The signal decay is a consequence of Doppler dephasing due to the velocity distribution along the direction of the grating vector. The modulation represents Larmor oscillations due to an external homogeneous magnetic field of ~3 G applied along the polarization direction of $\mathbf{k_1}$ beam[2].

The shape of the MGFID envelope is related to the velocity distribution of the atomic beam along the direction of the grating vector ($\Delta\mathbf{k}$), in particular, it has been established that the signal can be described by the effect of averaging over the velocity distribution of the sample [3,5,6]. The signal envelope is given by $e^{-(\Delta k u \theta/2)^2 t^2}$, where θ is the angle between the two traveling waves $\mathbf{k_1}$ and $\mathbf{k_2}$. Since the excitation pulses can be aligned so that the grating vector is oriented either parallel to atomic beam or transverse to it, it is possible to infer both the longitudinal and transverse velocity distributions of the beam by recording the decay time of the MGFID and the angle θ.

The results of preliminary experiments, which used a non-recirculating oven with the modified vacuum chamber, showed good agreement between the velocity distribution inferred from the MGFID and the geometry of the atomic beam [41]. In the following experiments that utilized the recirculating oven with the tube assembly as described in Section 3.3, we observed a significant improvement in the stability of the beam flux and signal to noise. However, there was a mismatch between the experimentally measured beam velocity obtained from spectroscopic measurements and the measured MGFID decay time. Figure 7 shows the MGFID amplitude as a function of time.

---

[2] Here and for all applicable signals in this section, the background trace is subtracted from the signal trace, the background trace is obtained by turning off the excitation pulse along $\mathbf{k_2}$.
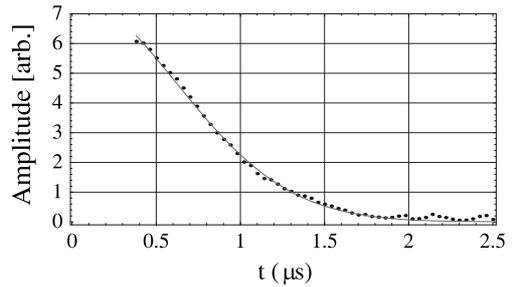
The excitation beams were aligned so that the grating vector is perpendicular to the atomic beam. A Gaussian fit to the data gives a decay time of ≈0.79 μs. The decay time can also be estimated from the longitudinal beam velocity $v_\parallel$ obtained from spectroscopic data (see Fig. 5). Alternatively, for the data shown in Figure 7, one can estimate the decay time from the atomic beam properties obtained from beam spectroscopy data. The most probable transverse velocity is given by $u \sim \alpha v_\parallel$, where α is an atomic beam divergence, whence the decay time is $\tau_d = 2\pi/ku\theta$. Given the beam geometry, we obtain $\tau_d \simeq 2$ μs. Therefore the MGFID lifetime obtained from the measured decay time is a factor 2.5 shorter than the prediction based on a measurement of the beam velocity. We attribute this discrepancy mainly to decoherence due to magnetic field gradients and imperfect overlap of nonuniform spatial profiles of excitation beams.

In contrast to the experiment with the coherence between the magnetic sublevels of the two hyperfine ground states described in references [42,43] where there was no linear differential Zeeman shift, we were not able to control the ambient magnetic field, which induced differential Zeeman shift along the atomic beam propagation direction. In our set-up no specific measures were taken to screen the ambient inhomogeneous magnetic field in part because the eventual goal of the apparatus was to explore the atomic density gratings that are insensitive to the magnetic fields. Long decay times are specifically desired for such gratings because the amplitude of the signal in this case falls of according to the power law of decay time and is zero at the exact fractional echo times [26,37].

Another mechanism of the discrepancy is related to inhomogeneity of profile of the two overlapped cylindrically shaped excitation beams with a ~30 mm waist along the atomic beam axis. To test this conjecture, we placed a narrow (≈5 mm) cardboard slit in front of the glass cell and observed the MGFID signal while scanning the slit across the laser beam profile. The lifetime of MGFID varied as we moved the slit, with the maximum corresponding to the position of the slit around the center of the laser beam cross section. The maximum of the duration of the decay observed through the slit experiment is 16% longer than the decay time observed without the slits. Thus the
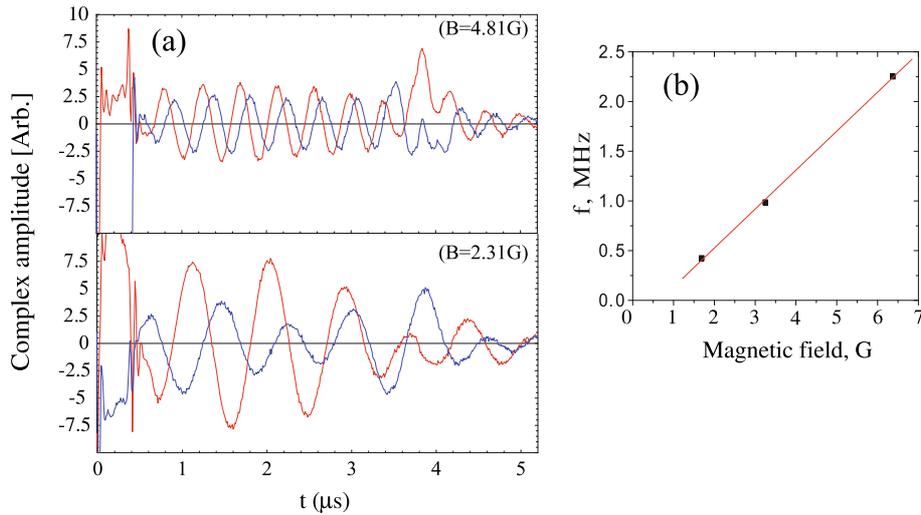
Fig. 8. (Color online) (a) MGFID in the presence of a homogeneous magnetic field. The first $\sim$400 ns correspond to the photodiode signal caused by the creation pulse itself; the spike at $\sim$3.7 μs is a secondary pulse due to AOM's imperfection; (b) the modulation frequency of the MGFID signal as a function of the applied magnetic field.

signals from various parts of the laser beam cross section contribute with different phases with respect to the local oscillator phase, causing the shortening of the decay time. We note that a relatively long spatial extent of the interaction beam is required for echo-type of experiments in time domain since the atoms need to be in the interaction region by the time of the second excitation pulse. For the practical application of atom deposition, this requirement does not apply since such an experiment will involve tightly focused laser fields that will be separated in space.

The shortening of the MGFID in the atomic beam, where the size of the atomic sample in the interaction region is of the order of few mm, is not surprising and shows that one needs a substantial control over the magnetic and laser fields on a macro scale as opposed to less stringent requirements in the similar experiments carried out with cold atoms in a MOT [12–14].

4.2 Effect of an external magnetic field

The data presented in the previous section shows the sensitivity of the MGFID and MGE to external magnetic fields. A homogeneous magnetic field modulates the MGFID signal with multiples of the Larmor frequency

$$\omega_L = \mu_B g_F B / \hbar,$$

where g_F is the total g-factor and μ_B is the Bohr magneton. The total g-factor is given by

$$g_F = g_J \frac{J(J+1) + F(F+1) - I(I+1)}{2F(F+1)},$$

where a much smaller nuclear term g_I is neglected, and g_J is the electron angular g-factor; F, J and I are, respectively, the total, electron, and nuclear angular momentum quantum numbers. Given all quantum numbers, one can calculate $g_F = 1/3$ for ^{85}Rb. The oscillation

frequency corresponds to the Zeeman shift between the magnetic sublevels. Therefore, in theory, the modulation frequency for our configuration ($\Delta m = 1$) is given by (0.468 MHz/G) $|\mathbf{B}|$.

To investigate the effect of the homogeneous magnetic field on the resulting coherence grating, we performed a series of experiments with a magnetic field created by a pair of Helmholtz coils. The **B**-field was aligned along the polarization of the $\mathbf{k_1}$ vector (a quantization axis). In Figure 8a we present the resulting traces of MGFID signals for various values of the external magnetic field. Here, the first 400 ns corresponds to saturation of the detection photodiodes; the large spikes in the signal traces at around 3.7 μs occur due to a secondary pulse, which results from the reflections of acoustic waves in AOM's crystal. The dependence of the modulation frequency on the applied magnetic field is plotted in Figure 8b. Each data point corresponds to the Fourier transform of the respective MGFID amplitude trace. As expected, the modulation frequency has a linear dependence on the magnetic field. From the linear fit we determined the modulation frequency of the MGFID per unit magnetic field to be $\approx$0.392 MHz/G. The obtained value is close to the expected value of 0.468 MHz/G for $\Delta m = 1$ coherence between ground state magnetic sublevels. The error is associated with a systematic uncertainty in our experiment due to magnetic coils calibration. The other part of the error comes from the inhomogeneity of the applied magnetic field and the magnetization of the stainless steel walls of the vacuum system. Despite the experimental uncertainty, the experimental data show that we indeed created coherences between the magnetic states that differ by $\Delta m = 1$. Fractional echo phenomena [27] should, in principle, lead to a formation of higher order coherence that correspond to Δm with higher integer number of multiple. A discussion of the improvement of precision measurements of g-factor up to 50 ppb using magnetic field modulation of MGFID in a cold Rb vapor was presented in a recent work [13].
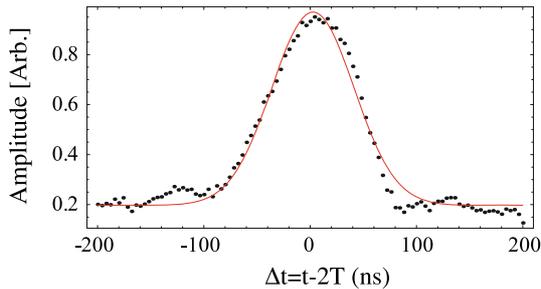
Fig. 9. (Color online) MGE signal experimental data and the fit to Gauss function with the decay time as a free parameter, the delay between pulses is $T = 1.8$ μs, duration of the pulses 200 ns, collimation aperture 7.5 mm. (Note, that the vertical scale does not relate to the scale used in the MGFID data.)

The equivalent experiment in a MOT in general provides a much longer interrogation time, which is crucial for such precision measurements.

4.3 Magnetic-grating echo

For practical applications it is desirable to extend the time scale, over which coherences can be observed. To overcome the relatively short MGFID duration associated with Doppler dephasing, we resort to the echo technique. The initially created coherence can be restored by applying a second excitation pulse at time $t = T$. The echo experiments were also carried out using traveling waves applied at a small angle. The resulting MGE signal has a much smaller amplitude than the MGFID signal because of requirements of effectively four-photon process. As shown in Figure 9, the signal reaches its maximum at the echo time of $t = 2T$. To distinguish the echo signal from background noise, we temporarily use an external magnetic field from permanent magnet to produce Larmor oscillations in the signal. In the actual experiment we varied pulse separation $T = 1.5-5$ μs. Figure 9 shows a typical MGE signal for a pulse separation of $T = 1.8$ μs. The data was obtained without laser cooling the atomic beam. A Gaussian function was used to fit to the MGE envelope. The MGE decay time obtained from the fit has the same time scale as the corresponding MGFID ($\sim$100 ns). The decay time corresponds to a relatively high transverse velocity distribution due to a larger collimation aperture used to increase the atomic flux. We were not able to systematically investigate MGE signals as the beam machine was partially disassembled at the time and the experimental goals were changed. However, the observation of the MGE indicates the possibility of utilizing high flux atomic beams to produce population grating echoes for generation of periodic patterns of atomic density.

5 Conclusion

In this paper, we presented experimental observation of coherence gratings in the time domain using a high flux thermal atomic beam. We showed that the gratings are associated with a superposition of magnetic sublevels of a single hyperfine ground state by studying the dynamics of the MGFID and MGE in external magnetic fields. We discussed factors that contributed to decoherence of the MGFID. We anticipate that goals related to atom deposition can be realized by extending the experiment to population grating echo technique and to include spatially separated excitation zones [2].

References

1. J.E. Bjorkholm, R.R. Freeman, A. Ashkin, D.B. Pearson, Phys. Rev. Lett. **41**, 1361 (1978)
2. B. Dubetsky, P.R. Berman, Phys. Rev. A **50**, 4057 (1994)
3. B. Dubetsky, P.R. Berman, Laser Phys. **4**, 1017 (1994)
4. B. Dubetsky, P.R. Berman, Appl. Phys. B **59**, 147 (1994)
5. U. Shim, S. Cahn, A. Kumarakrishnan, T. Sleator, Jin-Tae Kim, Jpn J. Appl. Phys. **41**, 3688 (2002)
6. U. Shim, S. Cahn, A. Kumarakrishnan, T. Sleator, Jin-Tae Kim, Jpn J. Appl. Phys. **44**, 168 (2005)
7. F. Bloch, W.W. Hansen, M. Packard, Phys. Rev. **70**, 474 (1946)
8. E.M. Purcell, H.C. Torrey, R.V. Pound, Phys. Rev. **69**, 37 (1946)
9. E.L. Hahn, Phys. Rev. **77**, 297 (1950)
10. E.L. Hahn, Phys. Rev. **80**, 580 (1950)
11. A.J.M. Kiruluta, J. Opt. Soc. Am. A **23**, 1391 (2006)
12. A. Kumarakrishnan, S.B. Cahn, U. Shim, T. Sleator, Phys. Rev. A **58**, R3387 (1998)
13. I. Chan, A. Andreyuk, S. Beattie, B. Barrett, C. Mok, M. Weel, A. Kumarakrishnan, Phys. Rev. A **78**, 033418 (2008)
14. A. Kumarakrishnan, U. Shim, S.B. Cahn, T. Sleator, Phys. Rev. A **58**, 3868 (1998)
15. J.H. Thywissen, M. Prentiss, New J. Phys. **7**, 47 (2005)
16. Hee Su Park, Sun Kyung Lee, Jae Yong Lee, Opt. Express **16**, 21982 (2008)
17. M. Kiffner, J. Evers, M.S. Zubairy, Phys. Rev. Lett. **100**, 073602 (2008)
18. For example, E. Arimondo, in *Progress in Optics XXXV*, edited by E. Wolf (Elsevier, Amsterdam, 1996), pp. 257−354
19. S.J. Bentley, R.W. Boyd, Opt. Express **12**, 5735 (2004)
20. G.S. Agarwal, K.T. Kapale, J. Phys. B: At. Mol. Opt. Phys. **39**, 3437 (2006)
21. N.A. Kurnit, I.D. Abella, S.R. Hartmann, Phys. Rev. Lett. **13**, 567 (1964)
22. I.D. Abella, N.A. Kurnit, S.R. Hartmann, Phys. Rev. **141**, 391 (1966)
23. N.N. Rubtsova, V.N. Ishchenko, E.B. Khvorostov, S.A. Kochubei, V.A. Reshetov, I.V. Yevseyev, Phys. Rev. A **70**, 023403 (2004)
24. E.A. Rotberg, B. Barrett, S. Beattie, S. Chudasama, M. Weel, I. Chan, A. Kumarakrishnan, J. Opt. Soc. Am. B **24**, 671 (2007)
25. A.A. Tonyushkin, Ph.D. Thesis, New York University, New York (2006)

26. S.B. Cahn, A. Kumarakrishnan, U. Shim, T. Sleator, P.R. Berman, B. Dubetsky, Phys. Rev. Lett. **79**, 784 (1997)
27. D.V. Strekalov, A. Turlapov, A. Kumarakrishnan, T. Sleator, Phys. Rev. A **66**, 023601 (2002)
28. G. Timp, R.E. Behringer, D.M. Tennant, J.E. Cunningham, M. Prentiss, K.K. Berggren, Phys. Rev. Lett. **69**, 1636 (1992)
29. J.J. McClelland, R.E. Scholten, E.C. Palm, R.J. Celotta, Science **262**, 877 (1993)
30. K.K. Berggren, A. Bard, J.L. Wilbur, J.D. Gillaspy, A.G. Heig, J.J. McClelland, S.L. Rolston, W.D. Phillips, M. Prentiss, G.M. Whitesides, Science **269**, 1255 (1995)
31. A. Camposeo, A. Piombini, F. Cervelli, F. Tantussi, F. Fuso, E. Arimondo, Opt. Commun. **200**, 231 (2001)
32. A. Camposeo, F. Cervelli, A. Piombini, F. Tantussi, F. Fuso, M. Allegrini, E. Arimondo, Mat. Sci. Eng. C **23**, 217 (2003)
33. C. O'Dwyer et al., Nanotechnology **16**, 1536 (2005)
34. R. Gupta, J.J. McClelland, P. Marte, R.J. Celotta, Phys. Rev. Lett. **76**, 4689 (1996)
35. Th. Schulze, B. Brezger, P.O. Schmidt, R. Mertens, A.S. Bell, T. Pfau, J. Mlynek, Mic. Eng. **46**, 105 (1999)
36. A. Turlapov, A. Tonyushkin, T. Sleator, Phys. Rev. A **71**, 043612 (2005)
37. A. Tonyushkin, T. Sleator, Phys. Rev. A **74**, 053615 (2006)
38. A. Tonyushkin, Phys. Rev. A **75**, 037602 (2007)
39. R.D. Swenumson, U. Even, Rev. Sci. Instrum. **52**, 559 (1981)
40. T.L. Gustavson, P. Bouyer, M.A. Kasevich, in *Methods for Ultrasensitive Detection*, Proc. of SPIE **3270**, 62 (1998)
41. A. Kumarakrishnan, A. Karpf, Z. Khaliq, D.V. Strekalov, A.V. Turlapov, T. Sleator, Bull. Am. Phys. Soc. **43**, 1296 (1998)
42. H.J. Lewandowski et al., Phys. Rev. Lett. **88**, 070403 (2002)
43. D.M. Harber et al., Phys. Rev. A **66**, 053616 (2002)